Supplementary Information for

# Controlling molecular assembly and charge transport of n-type organic semiconductors with sterically demanding substituents

Craig P. Yu[1], Naoya Kojima[2], Shohei Kumagai[1], Tadanori Kurosawa[1], Hiroyuki Ishii[3], Go Watanabe[4], Jun Takeya[1,2,5,6], and Toshihiro Okamoto[1,2,5,7*]

[1]Material Innovation Research Center (MIRC) and Department of Advanced Materials Science, School of Frontier Sciences, The University of Tokyo, 5-1-5 Kashiwanoha, Kashiwa, Chiba 277-8561, Japan

[2]Department of Applied Chemistry, Faculty of Engineering, The University of Tokyo, 7-3-1 Hongo, Bunkyo-ku, Tokyo 113-0033, Japan

[3]Department of Applied Physics, Faculty of Pure and Applied Sciences, University of Tsukuba, 1-1-1 Tennodai, Tsukuba, Ibaraki 305-8573, Japan

[4]Department of Physics, School of Science, Kitasato University, 1-15-1 Kitasato, Minami-ku, Sagamihara, Kanagawa 252-0373, Japan.

[5]National Institute of Advanced Industrial Science and Technology (AIST)-University of Tokyo Advanced Operando-Measurement Technology Open Innovation Laboratory (OPERANDO-OIL), AIST, 5-1-5 Kashiwanoha, Kashiwa, Chiba 277-8561, Japan

[6]International Center for Materials Nanoarchitectonics (MANA), National Institute for Materials Science (NIMS), 1-1 Namiki, Tsukuba 205-0044, Japan

[7]PRESTO, JST, 4-1-8 Honcho, Kawaguchi, Saitama 332-0012, Japan

*Corresponding Author:

Toshihiro Okamoto, tokamoto@k.u-tokyo.ac.jp

## 1. Synthetic Procedures

Synthesis of Ph–BQQDI

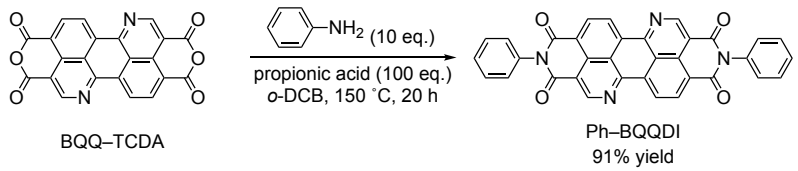


A flame-dried Schlenk tube was charged with **BQQ–TCDA** (117 mg, 0.297 mmol, 1.0 equiv.), aniline (275 mg, 2.96 mmol, 10.0 equiv.), propionic acid (2.00 mL, 297 mmol, 100 equiv.), and *o*-DCB (10.0 mL), and the mixture was stirred at 150 ˚C for 20 h under an atmosphere of argon. The resulting mixture was cooled to room temperature and precipitated in MeOH. The product was collected via vacuum filtration as a red solid (150 mg, 91%). **$^1$H NMR** (400 MHz, TCE-$d_2$): δ 9.74 (s, 2H), 9.39 (d, $J$ = 7.2 Hz, 2H), 8.93 (d, $J$ = 7.8 Hz, 2H), 7.53-7.62 (m, 6H), 7.38 (d, $J$ = 6.8 Hz, 4H). **HRMS** (APCI$^+$-TOF): Calcd for $C_{34}H_{28}N_4O_4$ [M+H] 545.1250, found 545.1271. **Elemental Analysis.** Calcd for $C_{34}H_{28}N_4O_4$: C, 75.00; H, 2.96; N, 10.29. Found: C, 74.92; H, 2.94; N, 10.12.

Synthesis of $Cy_6$–BQQDI

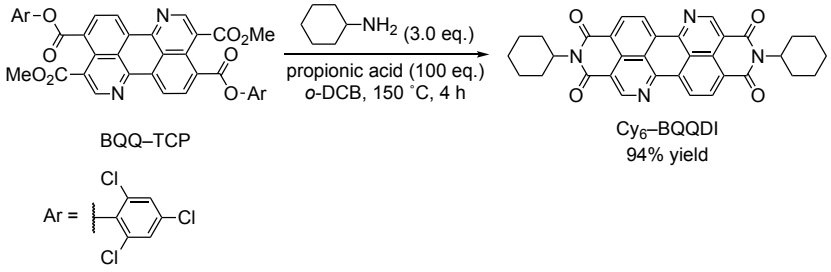


A flame-dried Schlenk tube was charged with **BQQ-TCP** (150 mg, 0.184 mmol, 1.0 equiv.), cyclohexylamine (54.6 mg, 0.551 mmol, 3.0 equiv.), and *o*-DCB (6.1 mL) and the reaction mixture was stirred at 150 °C for 1 h under an atmosphere of argon. After that, propionic acid (1.38 mL, 18.4 mmol, 100 equiv.) was added and the mixture was stirred at 150 °C for 3 h. The resulting mixture was cooled to room temperature and poured into a stirring solution of MeOH. The precipitates were collected via vacuum filtration to give the product as a red-purple solid (96.6 mg, 94%). **$^1$H NMR** (400 MHz, $CDCl_3$/HFIP-$d_2$): δ 9.58 (s, 2H), 9.28 (d, $J$ = 7.8 Hz, 2H), 8.83 (d, $J$ = 7.8 Hz, 2H), 4.96-5.02 (m, 2H), 2.42-2.52 (m, 4H), 1.92-1.95 (m, 4H), 1.75-1.78 (m, 6H), 1.29-1.51 (m, 6H). **HRMS** (APCI$^+$-TOF): Calcd for $C_{34}H_{28}N_4O_4$ [M+H] 557.2189,

found 557.2203 **Elemental Analysis.** Calcd for $C_{34}H_{28}N_4O_4$: C, 73.37; H, 5.07; N, 10.07, found: C, 73.24; H, 5.13; N, 9.99.

Synthesis of 4-Heptyl–BQQDI

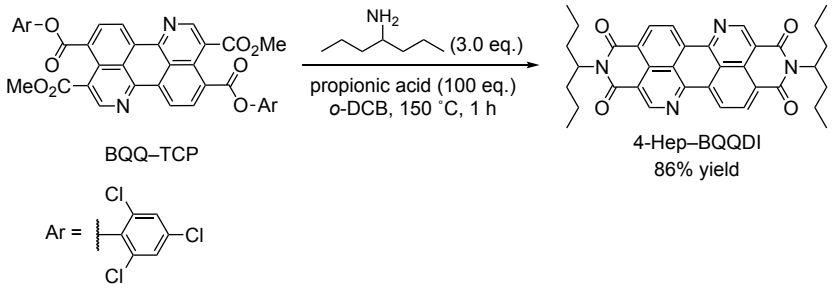


A flame-dried Schlenk tube was charged with **BQQ-TCP** (100 mg, 0.122 mmol, 1.0 equiv.), 4-heptylamine (42.3 mg, 0.367 mmol, 3.0 equiv.), propionic acid (0.912 mL, 12.2 mmol, 100 equiv.), and *o*-DCB (4.00 mL) the reaction mixture was stirred at 150 °C for 1 h under an atmosphere of argon. The resulting mixture was cooled to room temperature and poured into a stirring solution of MeOH. The precipitates were collected via vacuum filtration to give the product as a deep-red solid (61.7 mg, 86%). **$^1$H NMR** (400 MHz, $CDCl_3$/HFIP-$d_2$): δ 9.61 (s, 2H), 9.25 (d, $J$ = 7.6 Hz, 2H), 8.81 (d, $J$ = 8.0 Hz, 2H), 5.22-5.15 (m, 2H), 2.25-2.19 (m, 4H), 1.89-1.84 (m, 4H), 1.37-1.34 (m, 8H), 0.95-0.92 (m, 12H). **HRMS** (APCI$^+$-TOF): Calcd for $C_{36}H_{37}N_4O_4$ [M+H] 589.2815, found 589.2843. **Elemental Analysis.** Calcd for $C_{36}H_{37}N_4O_4$: C, 73.45; H, 6.16; N, 9.52, found: C, 73.23; H, 6.18; N, 9.39.

## 2. $^{1}$H NMR Spectra

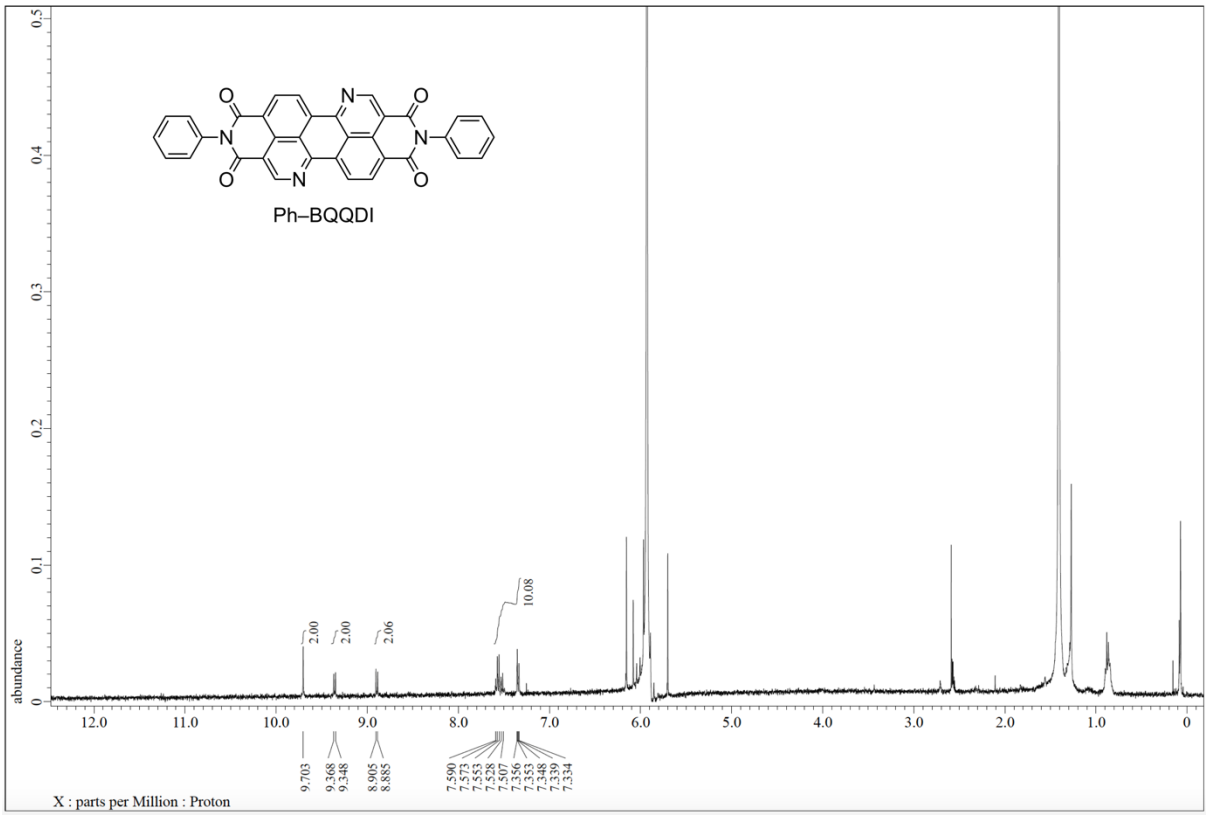


**Fig. S1**. The $^{1}$H NMR spectrum of **Ph–BQQDI** in TCE-$d_2$ at 100 ˚C.

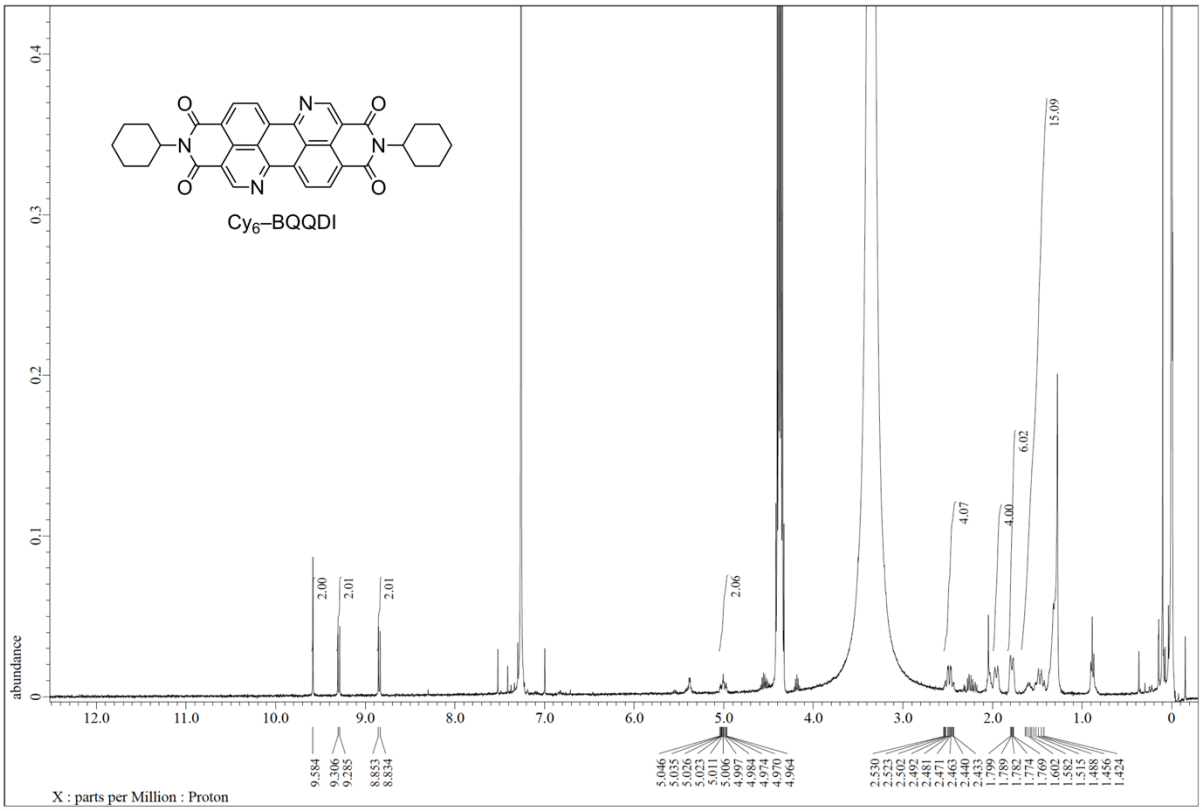


**Fig. S2**. The $^{1}$H NMR spectrum of **$Cy_6$–BQQDI** in $CDCl_3$/HFIP-$d_2$ at room temperature.

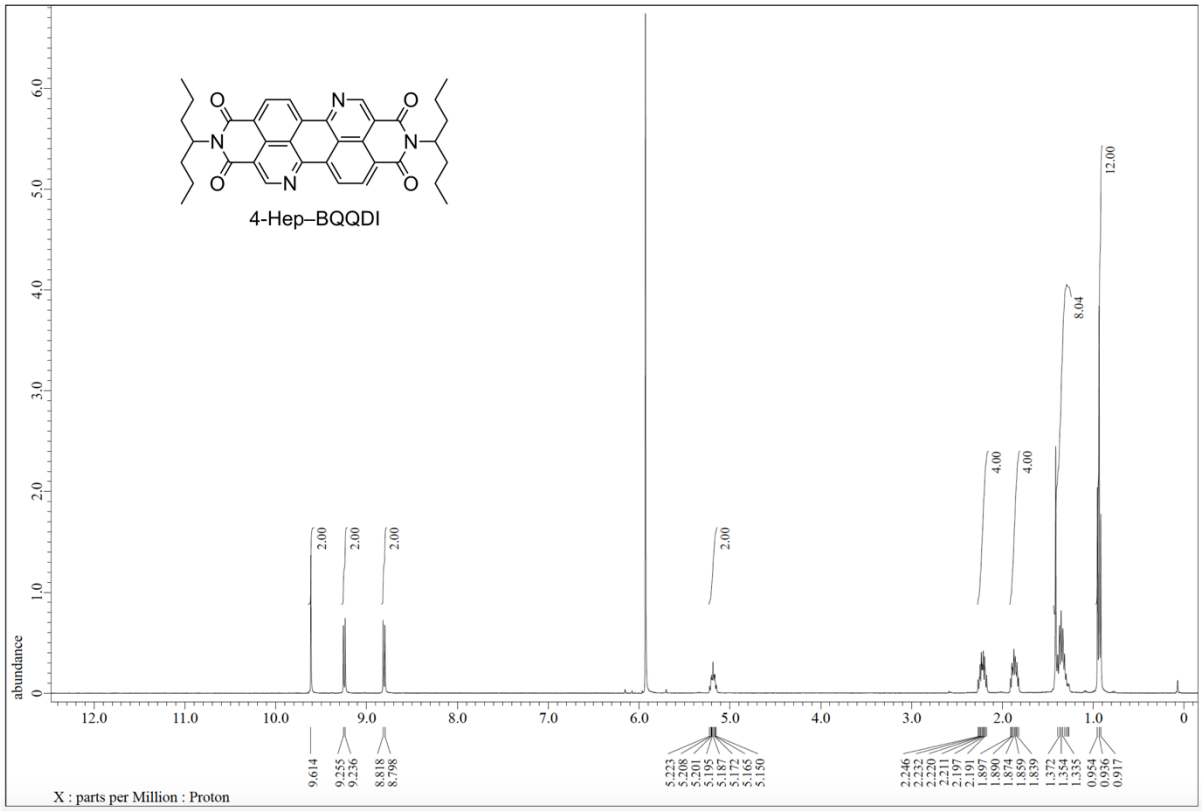


**Fig. S3**. The $^{1}$H NMR spectrum of **4-Heptyl–BQQDI** in TCE-$d_2$ at 100 ˚C.

## 3. Thermal Properties

Thermogravimetric−differential thermal analysis (TG−DTA) was performed on a Rigaku Thermo Plus EVO II TG 8121 at a heating rate of 1 K $min^{-1}$ under a nitrogen flow of 100 mL $min^{-1}$.

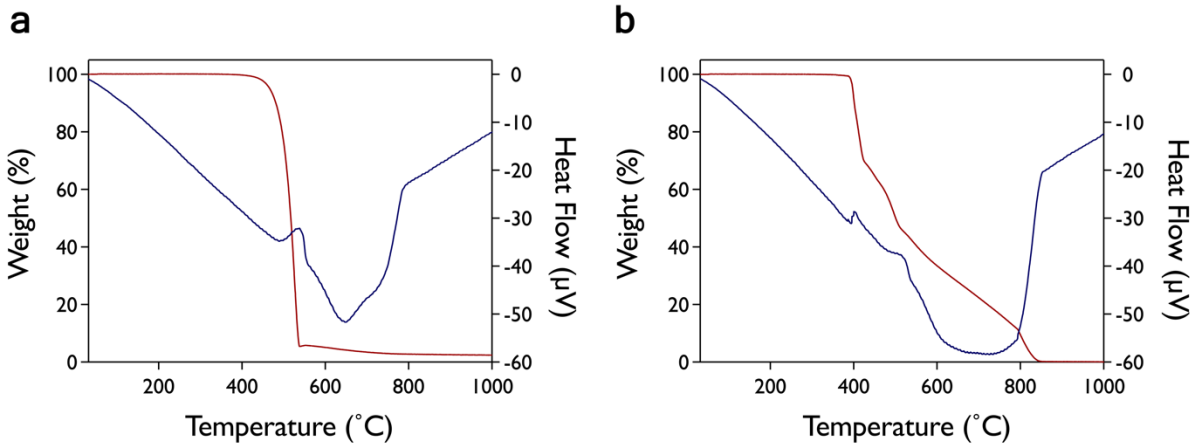


**Fig. S4**. TG-DTA curves of **a Ph–BQQDI**, and **b $Cy_6$–BQQDI**.

## 4. Solubility Tests

To a weighed sample of around 1 mg was added 200 μL of 1-chloronaphthalene, repeatedly. The resulting suspension was shaken and heated at 150 ˚C until complete dissolution. The total amount of solvent (mL) was converted into solubility in wt%.

**Table S1.** Solubility of **R–BQQDI**.

| Compound | Solubility (wt%) |
|---|---|
| **Ph$C_2$–BQQDI** | 0.038[1] |
| **$C_6$–BQQDI** | 0.20 |
| **$Cy_6$–BQQDI** | 0.0042 |
| **Ph–BQQDI** | < 0.001 |

## 5. X-Ray Crystallography

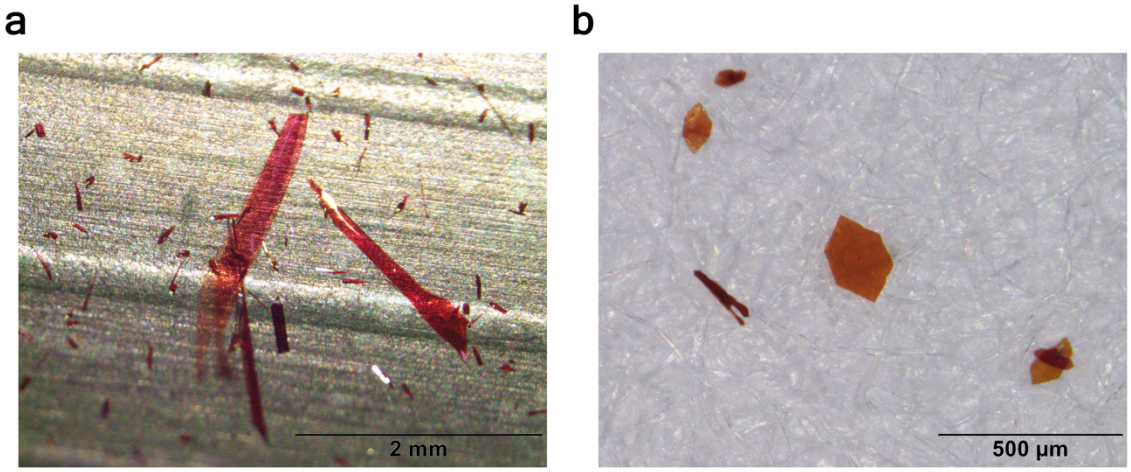


**Fig. S5**. Microscopic images of single-crystals of **a Ph–BQQDI**, and **b $Cy_6$–BQQDI**.

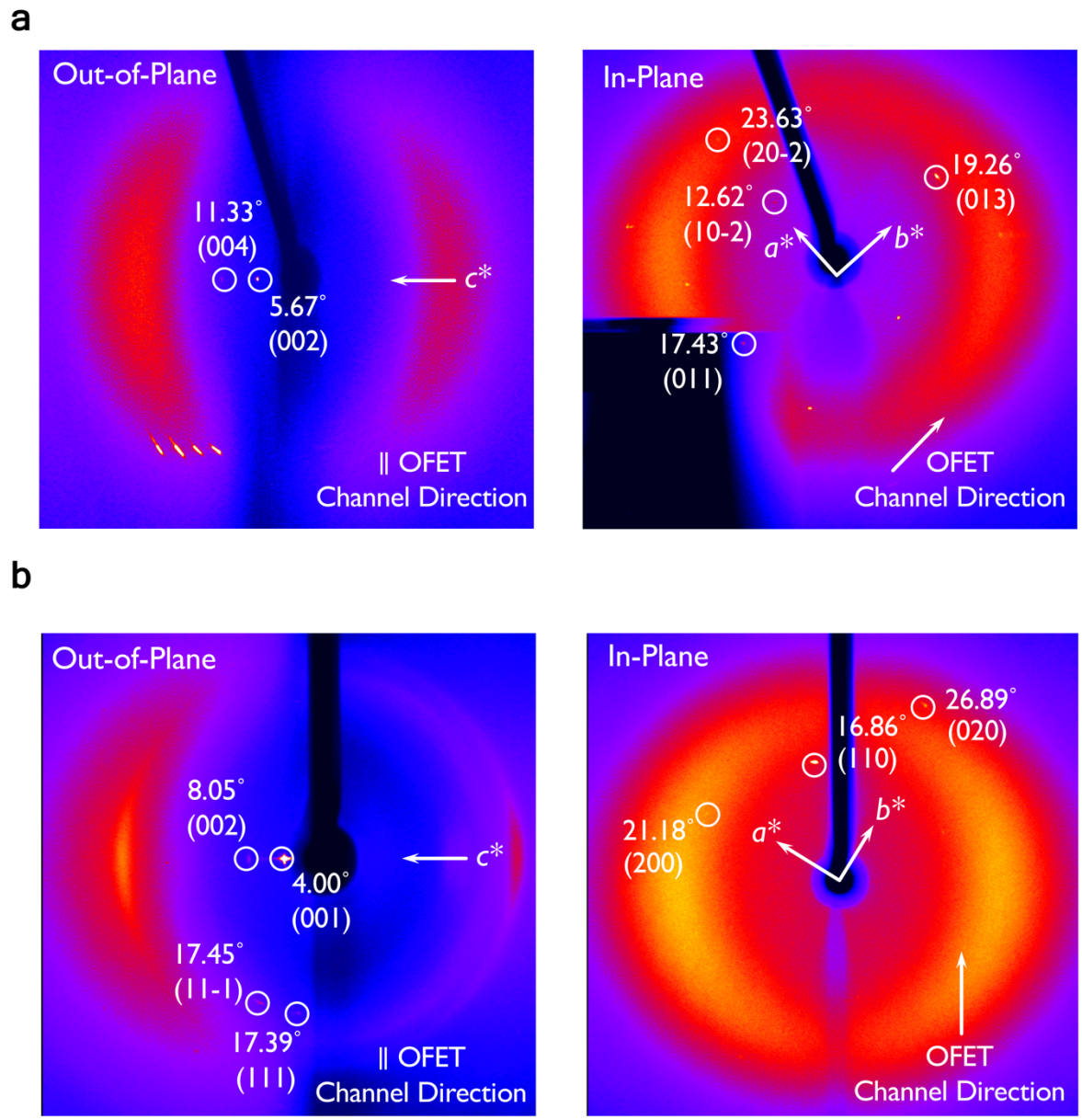


**Fig. S6**. Thin-film transmission X-ray diffraction images of **a Ph–BQQDI** and **b $Cy_6$–BQQDI**.

**Table S2.** Single-crystal data of **Ph–BQQDI** and **$Cy_6$–BQQDI**.

| **Material** | **Ph–BQQDI** | **$Cy_6$–BQQDI** |
|---|---|---|
| **Formula** | $C_{34}H_{16}N_4O_4$ | $C_{36}H_{30}N_2O_4$ |
| **Formula weight** | 544.52 | 556.62 |
| **Crystal system** | monoclinic | monoclinic |
| **Space group** | $P2_1/c$ | $C2/m$ |
| ***a* / Å** | 7.6097(4) | 8.5200(7) |
| ***b* / Å** | 5.1587(2) | 6.6538(6) |
| ***c* / Å** | 31.1537(14) | 22.3522(18) |
| ***α* / °** | 90 | 90 |
| ***β* / °** | 93.645(7) | 98.917(7) |
| ***γ* / °** | 90 | 90 |
| ***V* / Å$^3$** | 1220.50(10) | 1251.84(18) |
| ***Z*** | 2 | 2 |
| ***T* / K** | 298 | 297 |
| ***R*$_1$, *wR*$_2$ [*I* > 2*σ*(*I*)]** | 0.0682, 0.2098 | 0.0494, 0.1425 |
| ***R*$_1$, *wR*$_2$ [all data]** | 0.1214, 0.2341 | 0.0900, 0.1711 |
| **GOF** | 1.135 | 0.962 |

## 6. Molecular Dynamics Simulations

Molecular dynamics (MD) simulations of single crystal structures in this study were carried out by using the MD program GROMACS 2016. Since the intra- and interatomic interactions should be treated explicitly for analyzing the atomistic dynamics, an all-atom model was employed in accordance with generalized Amber force field parameters[2]. The partial atomic charges of the simulated molecules were calculated using the restrained electrostatic potential (RESP)[3] methodology, based on DFT calculations with the 6-31G(d) basis set using the GAUSSIAN 09 program[4].

For each system, the pre-equilibration run was initially performed at the given temperature for 5 ns after the steepest descent energy minimization. All systems were subjected to pre-equilibration runs in the NTV ensemble before their equilibration runs. During the pre-equilibration runs for the NTV ensemble, the Berendsen thermostat[5] was used to maintain the temperature of the system with relaxation time of 0.2 ps and the volume of the MD cell was kept constant. Subsequently, the NTP ensemble the equilibration run was performed using the Nosé-Hoover thermostat[6–8] and Parrinello-Rahman barostat[9] with relaxation times of 1.0 and 5.0 ps, respectively. For all MD simulations in the NTP ensemble, the pressure of the system was kept at 1.0 bar. The smooth particle-mesh Ewald (PME)[10] method was employed to treat the long-rang electrostatic interactions and the real space cutoff and the grid spacing are 1.2 and 0.30 nm, respectively. The time step was set to 1 fs.

To compare temperature dependence of thermal atomic fluctuations between different molecules, we calculated the B-factors related to the thermal stability as expressed below:

$$B = \frac{8}{3}\pi^2\Delta_i^2$$

where $\Delta_i$ is the root mean square fluctuations (RMSF) of atom $i$. The RMSF values can be estimated by using following equation:

$$\Delta_i = \sqrt{\frac{1}{T}\sum_{j=1}^{T}\left|\boldsymbol{r}_i(t_j) - \bar{\boldsymbol{r}}_i\right|^2}$$

where $T$ is the time step, $\boldsymbol{r}_i(t_j)$ is the position coordinate of atom $i$, and $\bar{\boldsymbol{r}}_i$ is the average of $\boldsymbol{r}_i(t_j)$. The RMSF values were analyzed from MD trajectories during the last 10 ns in the equilibrium.

## 7. Single-Crystalline OFET Fabrications and Evaluations

A highly $n^{++}$-doped silicon wafer was used as the substrate, which the surface was treated by a fluorinated insulating polymer, AL-X601 for **$Cy_6$–BQQDI**. The highly $n^{++}$-doped silicon wafer with thermally grown $SiO_2$ layer (200 nm) was ultrasonicated in acetone and isopropanol, and then dried on a hotplate in air. Following UV−$O_3$ treatment, AL-X601 diluted with propylene glycol monomethyl ether acetate (PGMEA) was spin-coated onto the wafer and baked at 150 °C for 5 min in an air, followed by curing at 180 °C for 10 min. Preparations of single-crystalline thin films were carried out by the solution-processed edge-casting method[10]. Thin-film crystals of **$Cy_6$–BQQDI** were grown from 0.015 wt% 1-chloronaphthalene solution at 140 °C. After the completion of crystallization, thin films were thoroughly dried in a vacuum oven at 100 °C for 10 hours. Then, 40 nm-thick gold layers were vacuum deposited through a metal shadow mask, acting as source and drain electrodes. Objective channel regions were edged by the conventional Nd:YAG laser etching technique. Before measurements, thermal annealing at 100 °C for 10 hours prior to electrical evaluations. The gate capacitance per unit area ($C_i$) for the AL-X601-containing gate dielectrics was measured to be 12.5 nF $cm^{-2}$ by a Keithley 4200-SCS.

Single crystals of **Ph−BQQDI** were prepared by the PVT technique with a two-zone furnace under an Ar flow at 80 $cm^3$ $min^{-1}$. High and low temperatures were set to 460 ˚C and 345 ˚C, respectively. Red platelet crystals were manually laminated onto an $n^+$-Si/$SiO_2$ (200 nm) substrate encapsulated by 200 nm-thick parylene layer, where $n^+$-Si and $SiO_2$/paryelene acted as a gate electrode and a gate insulator, respectively. 100 nm-thick Au layers, which were served as source and drain electrodes, were vacuum-deposited onto the laminated single crystal through a metal shadow mask. The gate capacitance per unit area ($C_i$) for the $SiO_2$/parylene was measured to be 8.83 nF $cm^{-2}$ by a Keithley 4200-SCS.

Electrical evaluations of OFETs were conducted on a Keithley 4200-SCS semiconductor parameter analyzer in air. Electron mobility and threshold voltage were extracted from the transfer characteristics by using the conventional equation for the saturation regime:

$$\sqrt{|I_D|} = \sqrt{\frac{W\mu_e C_i}{2L}}(V_G - V_{th}),$$

where $I_D$ is the drain current, $W$ the channel width, $\mu_e$ the electron mobility, $C_i$ the gate capacitance per unit area, $L$ the channel length, $V_G$ the gate voltage, and $V_{th}$ the threshold voltage.

## 8. Single-Crystalline Thin-Film OFET Performances

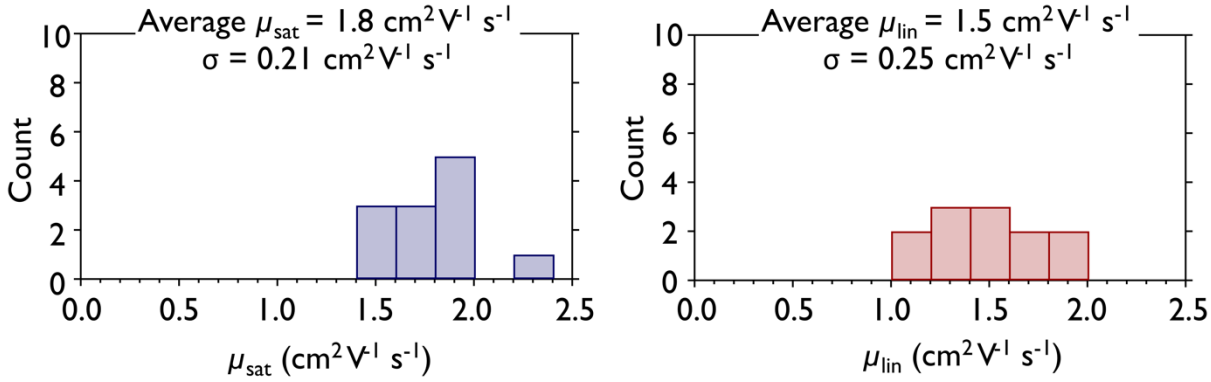


**Fig. S7**. Statistical distribution of $\mu_{sat}$ and $\mu_{lin}$ of **Cy$_6$–BQQDI**-based single-crystalline OFETs.

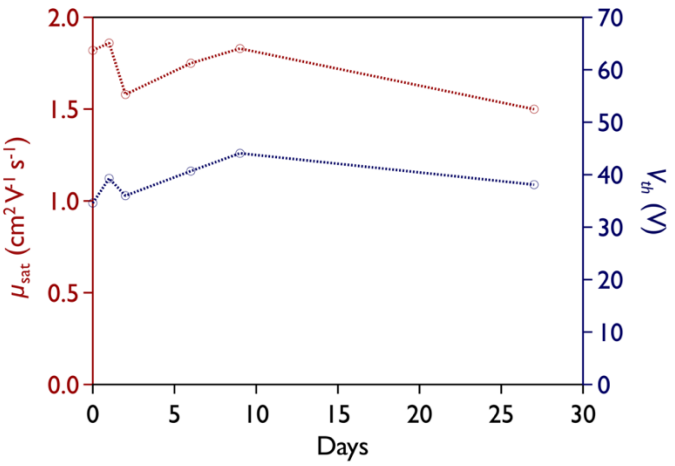


**Fig. S8**. Stability of $\mu_{sat}$ and $V_{th}$ of **Cy$_6$–BQQDI**-based single-crystalline OFETs.

## 9. Vacuum-Deposited Polycrystalline Thin-Film Fabrications and Evaluations

Vacuum-deposited 20 and 40 nm-thick polycrystalline thin films were used to produce top-contact, bottom-gate OFETs. For device fabrication, a highly $n^{++}$-doped silicon wafer with a thermally grown $SiO_2$ layer (200 nm) was used as a substrate, where the $SiO_2$ surface was modified with either decyltrimethoxysilane (DTS) or hexamethyldisilazane (HMDS). Before surface modification, the silicon wafer was washed by ultrasonication in acetone and isopropanol. After drying on a hotplate in air, the wafer was treated with UV−$O_3$. For DTS treatment, the wafer was exposed DTS vapour at 130 ˚C for 3 h, whereas HMDS was spin-coated, followed by annealing on a hotplate at 110 °C for 5 min, for HMDS treatment. The DTS-modified wafer was washed in toluene, acetone and isopropanol prior to use, whereas the HMDS-modified wafer was used immediately. Then, OSCs were vacuum-deposited at a rate of 0.5 Å $s^{-1}$ to form 40 nm-thick polycrystalline films, during which the substrates were kept at 180 ˚C. A gold coating was subsequently vacuum-evaporated through a shadow mask to obtain 60 nm-thick source and drain electrodes. Channel lengths ($L$) and widths ($W$) were 100 and 2000 μm, respectively, after patterning by the laser etching. Before evaluation, OFETs were thermally annealed at 60 ˚C for 10 h in a vacuum oven. Electrical evaluations of OFETs were conducted on a Keithley 4200-SCS semiconductor parameter analyzer in air. Electron mobility and threshold voltage were extracted from the transfer characteristics by using the conventional equation for the saturation regime:

$$\sqrt{|I_{\mathrm{D}}|} = \sqrt{\frac{W\mu_{\mathrm{e}}C_{\mathrm{i}}}{2L}}(V_{\mathrm{G}} - V_{\mathrm{th}})$$

where $I_{\mathrm{D}}$ is the drain current, $W$ the channel width, $\mu_{\mathrm{e}}$ the electron mobility, $C_{\mathrm{i}}$ the gate capacitance per unit area, $L$ the channel length, $V_{\mathrm{G}}$ the gate voltage, and $V_{\mathrm{th}}$ the threshold voltage.

## 10. Thin-Film Surface Morphology

Atomic force microscope (AFM) images were obtained using a Shimadzu SPM- 9700HT instrument in dynamic mode.

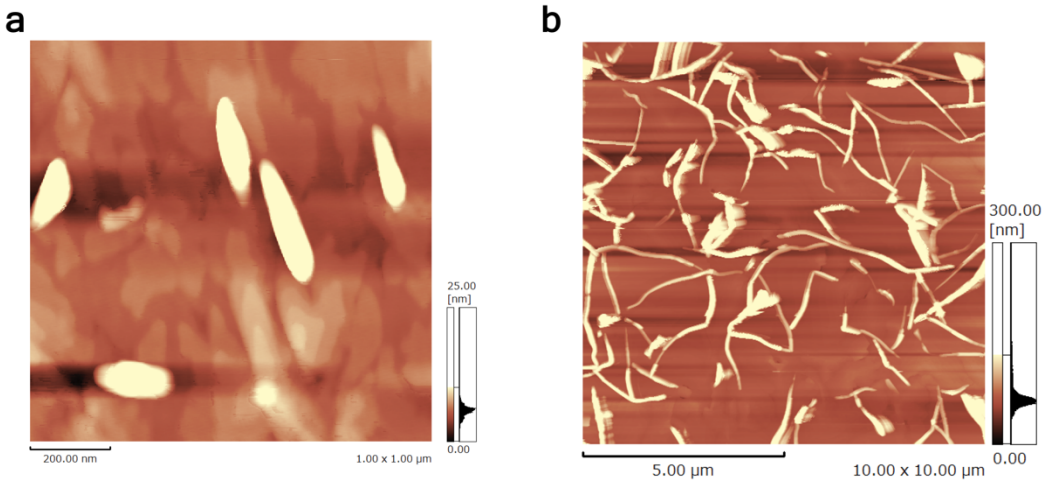


**Fig. S9**. AFM images of **a Ph–BQQDI** and **b Cy$_6$–BQQDI**, on DTS with thin-film thickness of 40 nm.

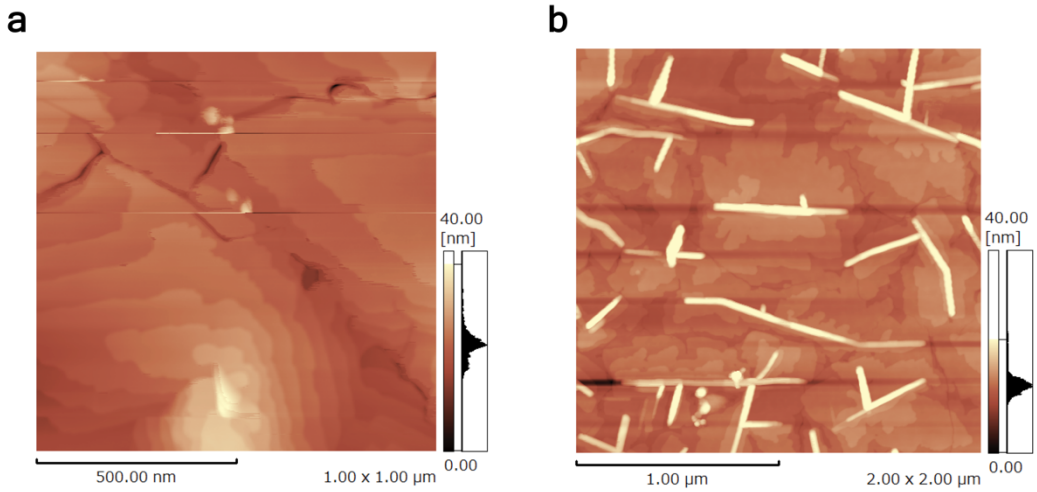


**Fig. S10**. AFM images of **Cy$_6$–BQQDI** on HMDS with thicknesses of **a** 40 nm and **b** 20 nm.

## 11. Polycrystalline Thin-Film Assemblies of Ph–BQQDI and $Cy_6$–BQQDI

Polycrystalline thin-film X-ray diffractions were collected by 2θ/ω scan on a Rigaku SmartLab diffractometer with a CuKα source (λ = 1.54056 Å).

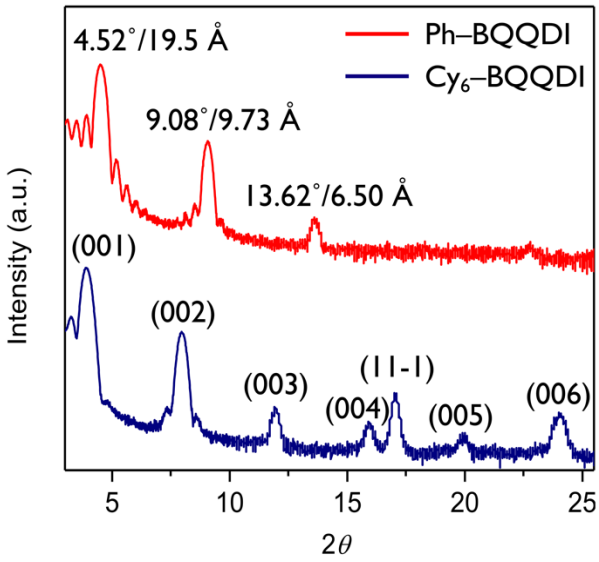


**Fig. S11**. Out-of-plane polycrystalline thin-film X-ray diffractions of **Ph–** and **$Cy_6$–BQQDI** on DTS.

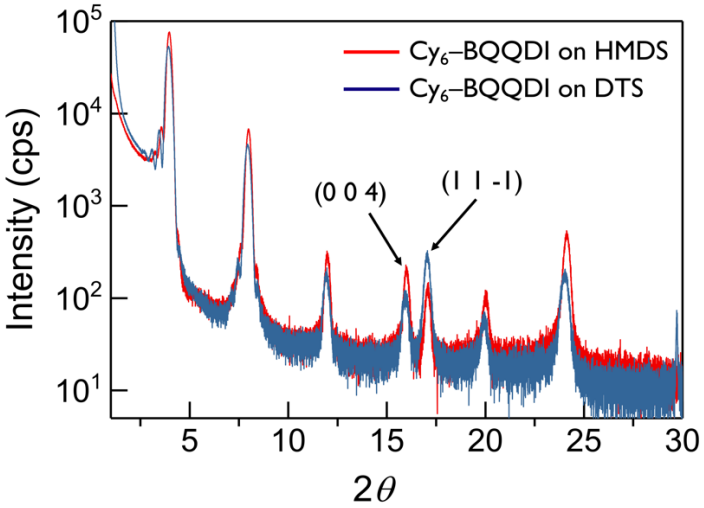


**Fig. S12**. Out-of-plane polycrystalline thin-film X-ray diffractions of **$Cy_6$–BQQDI** on DTS and HMDS.

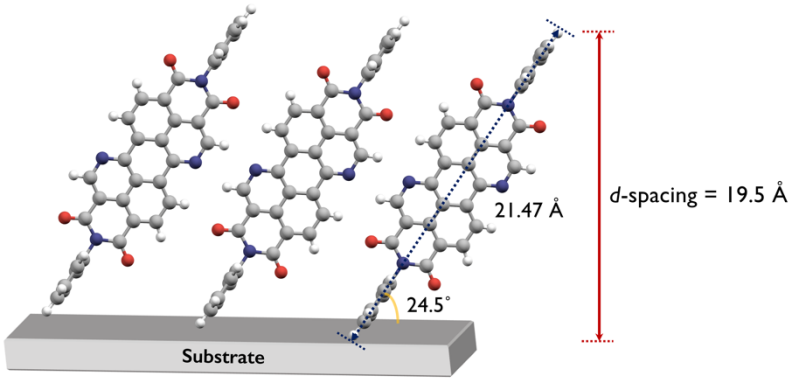


**Fig. S13**. The tilting angle of **Ph–BQQDI** thin-film assembly on the OFET substrate.

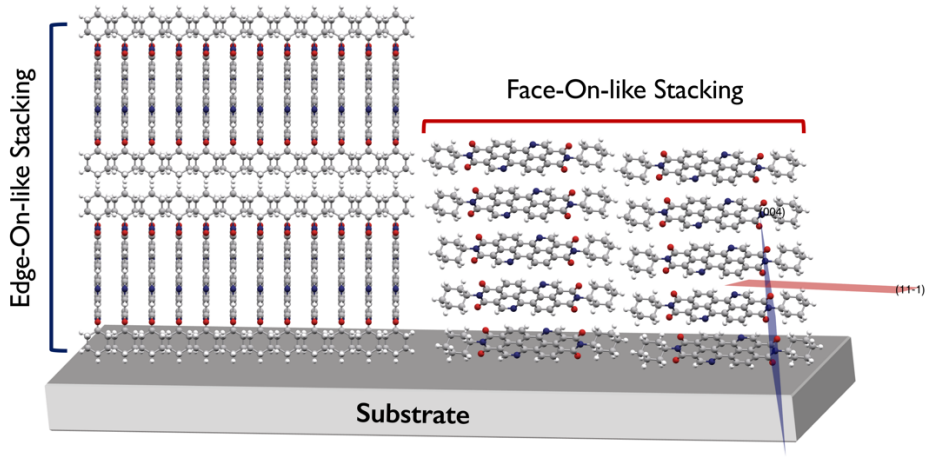


**Fig. S14**. Edge-on and face-on-like stacking of polycrystalline **$Cy_6$–BQQDI** on the OFET substrate.

## 12. Polycrystalline Thin-Film OFET Performances

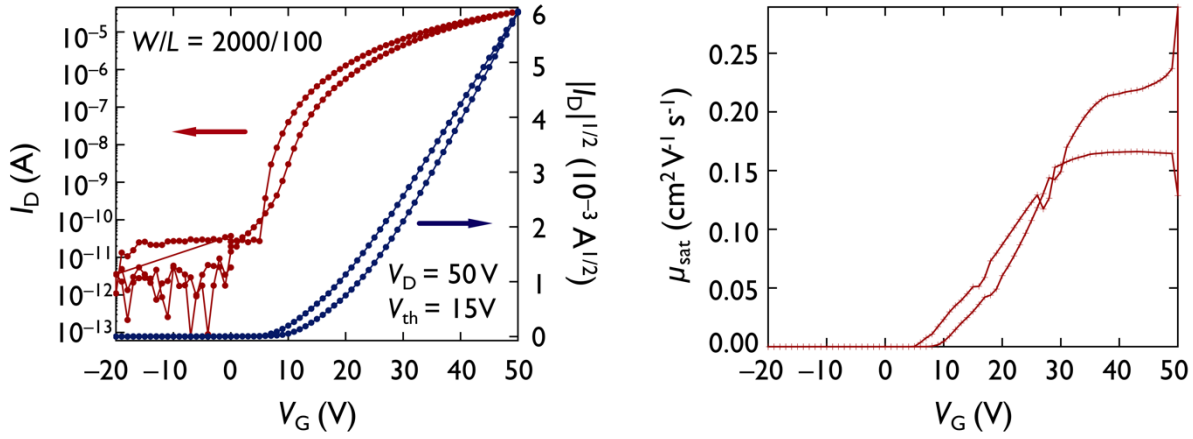


**Fig. S15**. Transfer characteristics and $\mu_{sat}$ of 40 nm-thick **Ph–BQQDI** polycrystalline OFET on DTS.

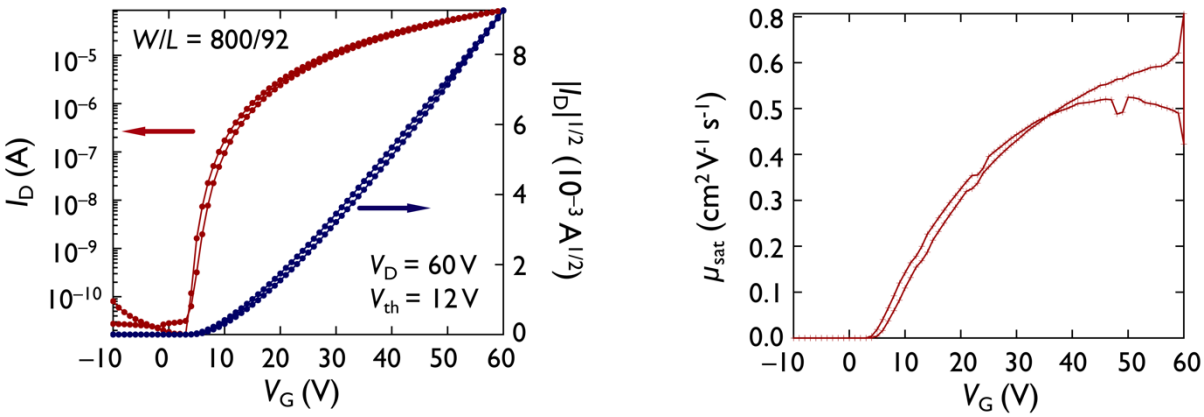


**Fig. S16**. Transfer characteristics and $\mu_{sat}$ of 40 nm-thick **$Cy_6$–BQQDI** polycrystalline OFET on DTS.

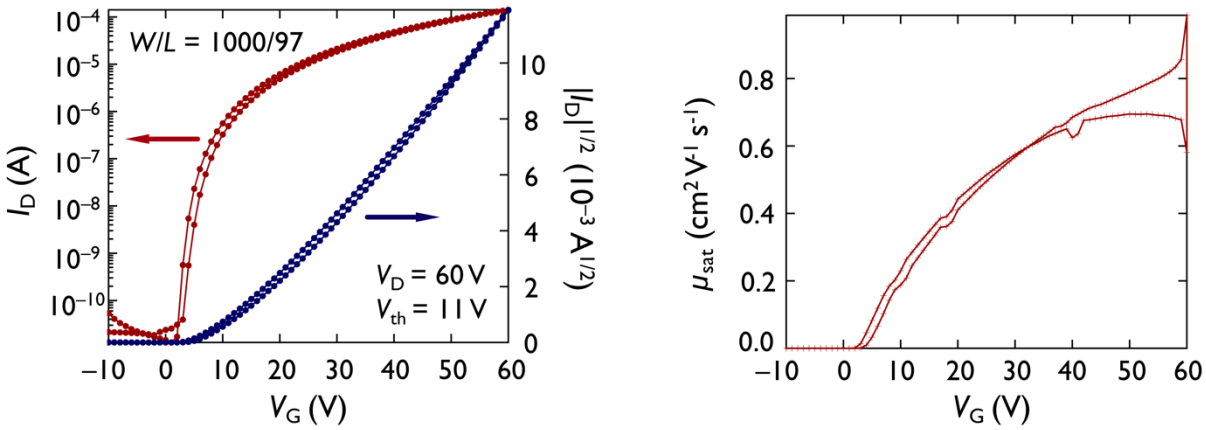


**Fig. S14**. Transfer characteristics and $\mu_{sat}$ of 40 nm-thick **$Cy_6$–BQQDI** polycrystalline OFET on HMDS.

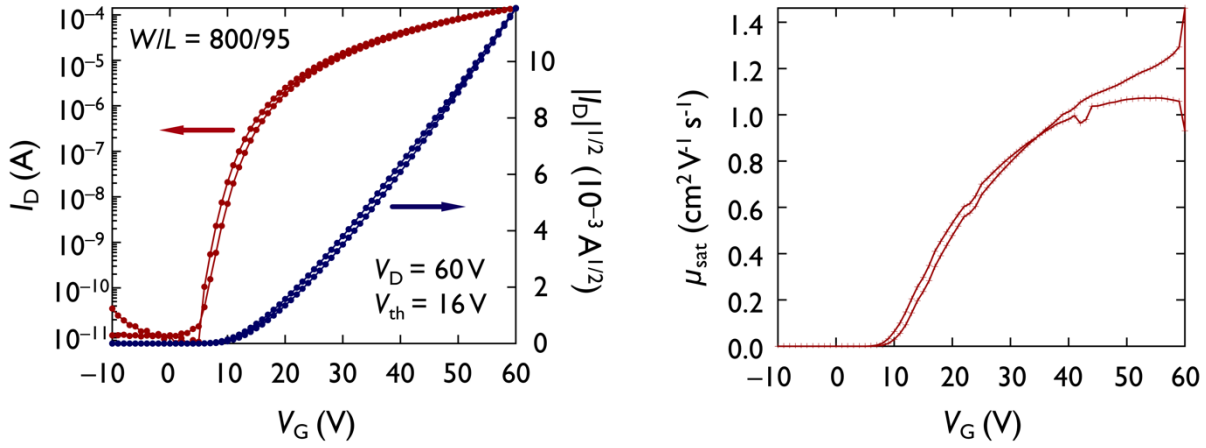


**Fig. S17**. Transfer characteristics and $\mu_{sat}$ of 20 nm-thick **$Cy_6$–BQQDI** polycrystalline OFET on HMDS with a channel length of 100 µm.

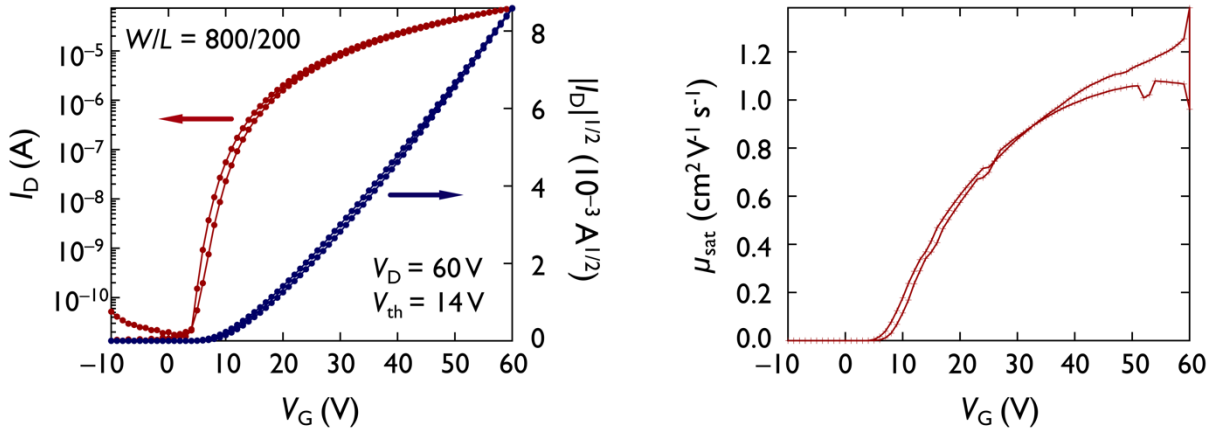


**Fig. S18**. Transfer characteristics and $\mu_{sat}$ of 20 nm-thick **Cy$_6$–BQQDI** polycrystalline OFET on HMDS with a channel length of 200 µm.

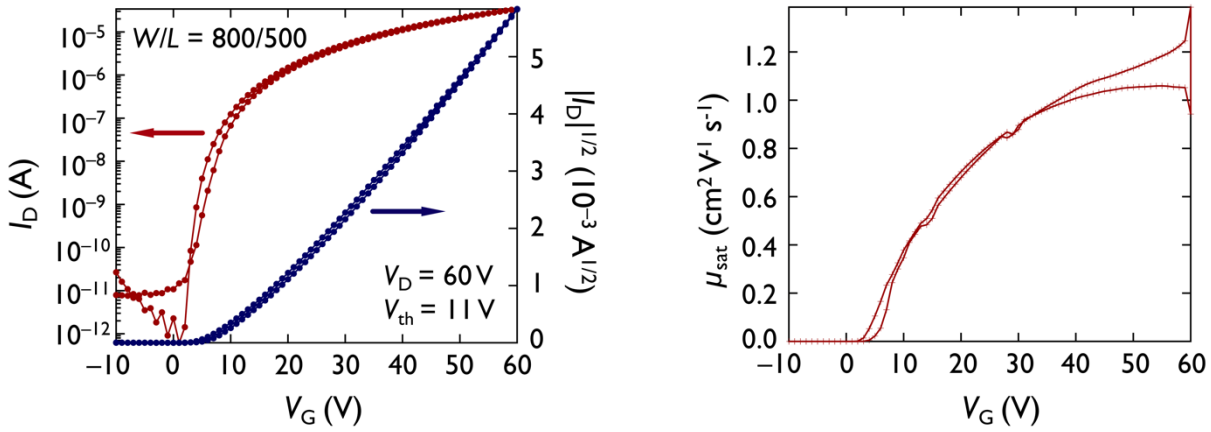


**Fig. S19**. Transfer characteristics and $\mu_{sat}$ of 20 nm-thick **Cy$_6$–BQQDI** polycrystalline OFET on HMDS with a channel length of 500 µm.

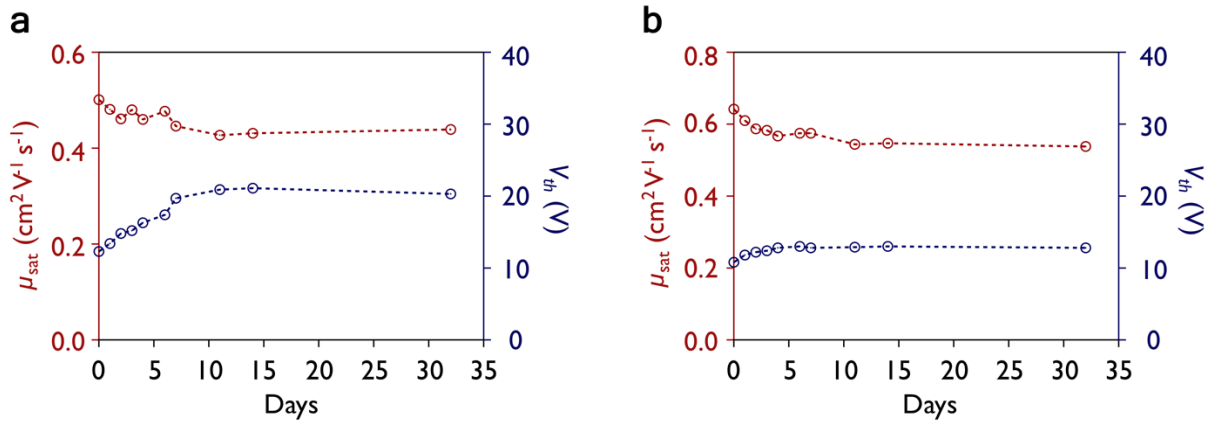


**Fig. S20**. Stability of $\mu_{sat}$ and $V_{th}$ of 40 nm-thick **Cy$_6$–BQQDI**-based polycrystalline OFETs on **a** DTS and **b** HMDS.

## 13. 2D LUMO Bands

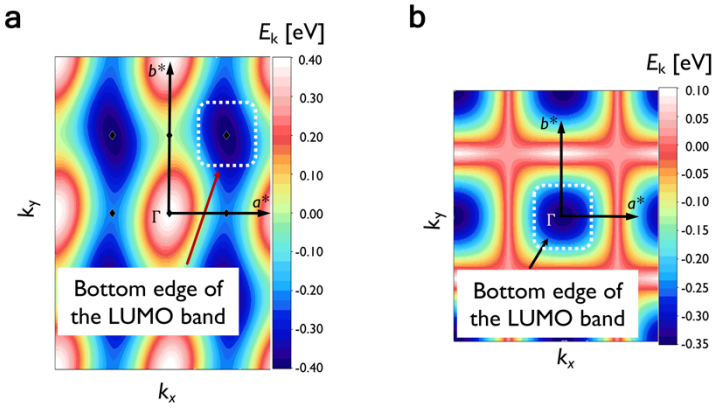


**Fig. S21**. Bottom edges of the 2D LUMO bands for **a Ph–BQQDI** and **b $Cy_6$–BQQDI** that effective mass values are calculated from.

## 14. References


1. Okamoto, T. *et al.* Robust, high-performance n-type organic semiconductors. *Sci. Adv.* **6**, eaaz0632 (2020).

2. Wang, J., Wolf, R. M., Caldwell, J. W., Kollman, P. A. & Case, D. A. Development and testing of a general Amber force field. *J. Comput. Chem.* **25**, 1157–1174 (2004).

3. Bayly, C. I., Cieplak, P., Cornell, W. D. & Kollman, P. A. A well-behaved electrostatic potential based method using charge restraints for deriving atomic charges: The RESP model. *J. Phys. Chem.* **97**, 10269–10280 (1993).

4. Frisch, M. J. et al. Gaussian 09, Revision A.02. *Gaussian 09, Revision A.02* (2009).

5. Berendsen, H. J. C., Postma, J. P. M., Van Gunsteren, W. F., Dinola, A. & Haak, J. R. Molecular dynamics with coupling to an external bath. *J. Chem. Phys.* **81**, 3684–3690 (1984).

6. Nosé, S. A unified formulation of the constant temperature molecular dynamics methods. *J. Chem. Phys.* **81**, 511–519 (1984).

7. Nosé, S. A molecular dynamics method for simulations in the canonical ensemble. *Mol. Phys.* **52**, 255–268 (1984).

8. Hoover, W. G. Canonical dynamics: Equilibrium phase-space distributions. *Phys. Rev. A* **31**, 1695–1697 (1985).

9. Parrinello, M. & Rahman, A. Polymorphic transitions in single crystals: A new molecular dynamics method. *J. Appl. Phys.* **52**, 7182–7190 (1981).

10. Darden, T., York, D. & Pedersen, L. Particle mesh Ewald: An N·log(N) method for Ewald sums in large systems. *J. Chem. Phys.* **98**, 10089–10092 (1993).

11. Uemura, T., Hirose, Y., Uno, M., Takimiya, K. & Takeya, J. Very high mobility in solution-processed organic thin-film transistors of highly ordered [1]benzothieno[32-b]benzothiophene derivatives. *Appl. Phys. Express* **2**, 111501 (2009).